Letters

3.5-kW 94.2% DC–DC Efficiency Capacitive Power Transfer With Zero Reactive Power Circulating

Yao Wang, *Student Member, IEEE*, Hua Zhang, *Member, IEEE*, and Fei Lu, *Member, IEEE*

***Abstract*—Most existing capacitive power transfer (CPT) circuits are developed from basic series–series CPT compensation, which have a common drawback of unavoidable reactive power circulating from the primary side of the capacitive coupler to its secondary side, causing reactive power loss, weakening power transfer capability, and aggravating electric field emission. To solve these concerns, this letter proposed a parallel–parallel (PP) compensation-based CPT system with double-side series–parallel (SP) inductive power transfer (IPT) links. The PP CPT compensation aims at zero reactive power circulating while the SP IPT links achieve high-power transfer capability. A 2.5-MHz prototype is implemented, and experiments validate the zero reactive power circulating property with 3.55 kW output power at a 94.2% dc–dc efficiency, and the peak efficiency achieves 94.6% at 1.62 kW output power. This letter is accompanied by slides as multimedia material demonstrating the motivations, contributions, and advantages over existing state-of-the-art CPT designs.**

***Index Terms*—Capacitive power transfer (CPT), parallel–parallel (PP) compensation, series–parallel (SP) inductive power transfer (IPT) link, zero reactive power circulating.**

I. Introduction

DUE to its lightweight, high misalignment tolerance, and no eddy-current loss, capacitive power transfer (CPT) technology is becoming an alternative to the traditional inductive power transfer (IPT) approach [1], [2], [3].

The double-sided *LC* circuit uses two series inductors, which is considered a basic series–series (SS) compensation [4]. Most existing CPT circuits are developed from the basic SS compensation [3], [4], [5], [6], [7], [8], [9], of which the structure is shown in Fig. 1. For example, the double-side *LCLC* and *CLLC* circuits are built by SS compensation, and additional T-type *LCL* and *CLC* networks, respectively [5], [6]. However, the SS-based CPT circuits have a common drawback of unavoidable reactive power circulating from the primary side of the capacitive coupler to its secondary side, typically causing the following three issues:

1) reactive power loss on the coupler;
2) weakened power transfer capability;
3) aggravated electric field (E-field) at a given power.

The equivalent capacitive coupler model and description are presented in Fig. 2 and Table I. In Fig. 2(b), only when self-capacitances C_1 and C_2 are fully compensated can the circulated reactive power Q_{12} be eliminated, and the transferred active power P_{12} be maximized. Among four basic compensations, SS, series–parallel (SP), parallel–series (PS), and parallel–parallel (PP) [10], only the PP compensation can achieve such a design. Therefore, a PP compensation-based CPT circuit structure is developed, as shown in Fig. 3. With double-side SP IPT links proposed as high-order compensation, an M_1-*PP*-M_2 CPT system is demonstrated in Fig. 4. The double-sided SP IPT links are

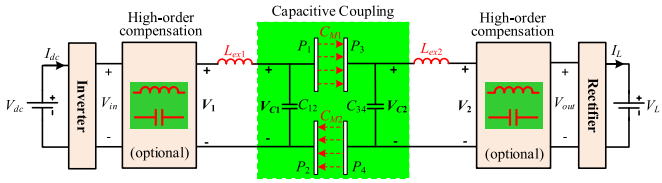

Fig. 1. Existing SS compensation-based CPT circuit structure.

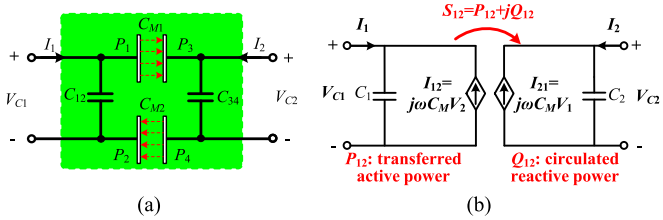

Fig. 2. (a) Equivalent circuit of CPT coupler. (b) Equivalent behavior-source model.

TABLE I
DESCRIPTION OF CPT

Parameter	Definition
Mutual capacitance C_M	$C_M=(C_{M1}C_{M2})/(C_{M1}+C_{M2})$
Self-capacitance C_1, C_2	$C_1=C_{12}+C_M$, $C_2=C_{34}+C_M$
Coupling coefficient k_C	$k_C=C_M/(C_1C_2)^{0.5}$

Manuscript received 25 July 2022; revised 26 August 2022 and 20 September 2022; accepted 13 October 2022. Date of publication 17 October 2022; date of current version 18 November 2022. This work was supported by the Advanced Research Projects Agency-Energy, U.S. Department of Energy, through BREAKERS program, monitored by Dr. Isik Kizilyalli, under Grant DE-AR0001114. *(Corresponding author: Fei Lu.)*

Yao Wang and Fei Lu are with the Department of Electrical and Computer Engineering, Drexel University, Philadelphia, PA 19104 USA (e-mail: yw696@drexel.edu; fei.lu@drexel.edu).

Hua Zhang is with the Department of Electrical Engineering, Rowan University, Glassboro, NJ 08028 USA (e-mail: hua.zhang@drexel.edu).

This article has supplementary material provided by the authors and color versions of one or more figures available at https://doi.org/10.1109/TPEL.2022.3215283.

Digital Object Identifier 10.1109/TPEL.2022.3215283

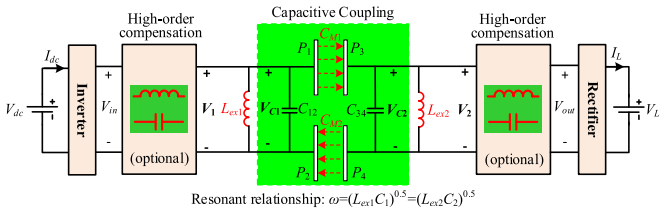

Fig. 3. Proposed PP compensation-based CPT circuit structure.

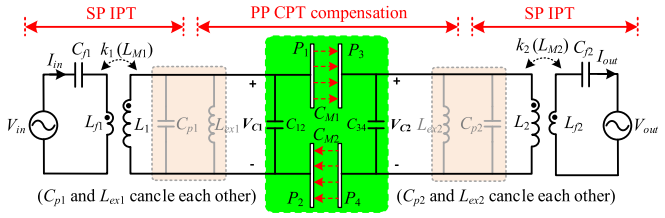

Fig. 4. Proposed PP CPT circuit with double-side SP IPT links, namely M_1-*PP*-M_2 system (C_{p1}, L_{ex1}, C_{p2}, and L_{ex2} can be cancelled due to parallel resonance).

used to boost the port voltages V_{C1} and V_{C2} of the capacitive coupler, enabling high-power transfer.

There are three innovations in the proposed CPT circuit.

1) First, zero reactive power circulating is achieved, reducing the power loss and maximizing power transfer capability.
2) Second, zero reactive power circulating is immune to the variations of coupling coefficient and load conditions.
3) Third, the voltage stress and E-field emission of the capacitive coupler are minimized under given working conditions.

II. Comparison Between SS and PP CPT Compensations

A. Power Flow Analysis

According to Fig. 2(b), the power flow S_{12} in a capacitive coupler can be calculated, as shown in the following:

$$\begin{aligned}\boldsymbol{S}_{12} &= \boldsymbol{V}_{C1}\cdot(-\boldsymbol{I}_{12}^{*}) \\ &= \omega C_M V_{C1} V_{C2}\sin\varphi_{21} + j\omega C_M V_{C1} V_{C2}\cos\varphi_{21}. \end{aligned} \quad (1)$$

where φ_{21} is the phase difference between $\boldsymbol{V_{C2}}$ and $\boldsymbol{V_{C1}}$. The transferred active power P_{12} and circulated reactive power Q_{12} are

$$\begin{cases} P_{12} = \mathrm{Re}[\boldsymbol{S}_{12}] = V_{C1}V_{C2}\omega C_M \sin\varphi_{21} \\ Q_{12} = \mathrm{Im}[\boldsymbol{S}_{12}] = V_{C1}V_{C2}\omega C_M \cos\varphi_{21}. \end{cases} \quad (2)$$

It indicates that both P_{12} and Q_{12} relate to φ_{21}. When φ_{21} is 90°, the transferred active power P_{12} is maximized, and zero reactive power circulating ($Q_{12}=0$) is realized.

B. Reactive Power Comparison in SS and PP Compensations

Two basic CPT compensations, SS and PP CPT circuits, are shown in Fig. 5, which have been analyzed in [10]. The working properties of zero-phase angle (ZPA) resonant frequency, load-independent output, etc., are summarized in Table II. $\boldsymbol{V_1}$ and $\boldsymbol{V_2}$ are the input and output voltages with 90° out of phase [10]. $\boldsymbol{V_{C1}}$ and $\boldsymbol{V_{C2}}$ are port voltages of the coupler.

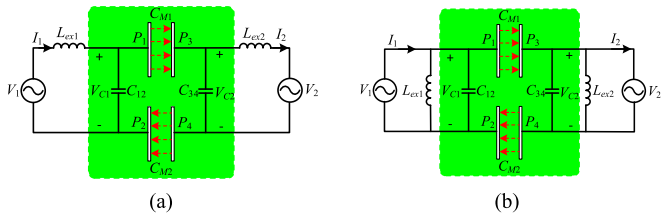

Fig. 5. (a) SS CPT compensation. (b) PP CPT compensation.

TABLE II
Working Properties of SS and PP CPT Compensations [10]

Property	SS CPT compensation	PP CPT compensation
ZPA resonance	$\omega=\frac{1}{\sqrt{L_{ex1}C_1(1-k_C^2)}}=\frac{1}{\sqrt{L_{ex2}C_2(1-k_C^2)}}$	$\omega=\frac{1}{\sqrt{L_{ex1}C_1}}=\frac{1}{\sqrt{L_{ex2}C_2}}$
Input/output current	$\begin{cases}\boldsymbol{I}_1=\boldsymbol{V}_2\cdot j\omega C_M(1/k_C^2-1)\\ \boldsymbol{I}_2=-\boldsymbol{V}_1\cdot j\omega C_M(1/k_C^2-1)\end{cases}$	$\begin{cases}\boldsymbol{I}_1=-\boldsymbol{V}_1\cdot j\omega C_M\\ \boldsymbol{I}_2=\boldsymbol{V}_1\cdot j\omega C_M\end{cases}$
Input/output voltage	$V_1=V_1\angle 0°,\ \boldsymbol{I}_1=I_1\angle 0°$ $V_2=V_2\angle -90°,\ \boldsymbol{I}_2=I_2\angle -90°$	$V_1=V_1\angle 0°,\ \boldsymbol{I}_1=I_1\angle 0°$ $V_2=V_2\angle 90°,\ \boldsymbol{I}_2=I_2\angle 90°$
Coupler voltages	$\begin{cases}\boldsymbol{V}_{C1}=\boldsymbol{V}_1-\boldsymbol{I}_1 j\omega L_{ex1}\\ \boldsymbol{V}_{C2}=\boldsymbol{V}_2+\boldsymbol{I}_2 j\omega L_{ex2}\end{cases}$	$\begin{cases}\boldsymbol{V}_{C1}=\boldsymbol{V}_1\\ \boldsymbol{V}_{C2}=\boldsymbol{V}_2\end{cases}$

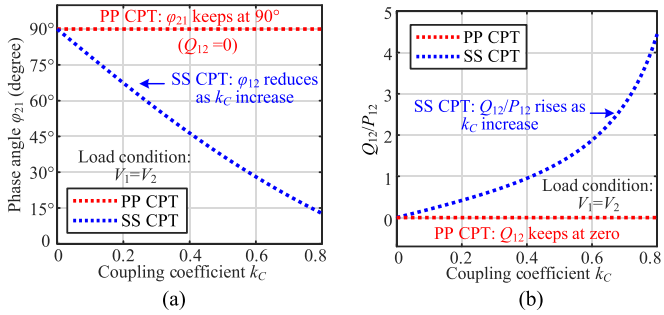

Fig. 6. Comparison between SS and PP compensation in (a) φ_{21} and (b) Q_{12}/P_{12}.

In an SS CPT compensation, the phase angles of $\boldsymbol{V_{C1}}$ and $\boldsymbol{V_{C2}}$ are defined as φ_1 and φ_2. Assuming $L_{ex1}=L_{ex2}$ and $C_1=C_2$, according to Table II, φ_1 and φ_2 are calculated as follows:

$$\begin{cases}\varphi_1 = -\arctan\frac{I_1\omega L_{ex1}}{V_1} = -\arctan\left(\frac{V_2}{V_1}\cdot\frac{1}{k_C}\right)\\ \varphi_2 = -90°+\arctan\frac{I_2\omega L_{ex2}}{V_2} = -90°+\arctan\left(\frac{V_1}{V_2}\cdot\frac{1}{k_C}\right).\end{cases} \quad (3)$$

Therefore, in an SS CPT compensation, φ_{21} is given as

$$\begin{aligned}\varphi_{21}|_{SS} &= \varphi_2-\varphi_1 \\ &= \arctan\left(\frac{V_2}{V_1}\cdot\frac{1}{k_C}\right)+\arctan\left(\frac{V_1}{V_2}\cdot\frac{1}{k_C}\right)-90°.\end{aligned} \quad (4)$$

In an SS CPT, φ_{21} is related to coupling coefficient k_C and load condition V_2/V_1. When $V_1=V_2$, φ_{21} is shown in Fig. 6(a), meaning it reduces as k_C rises. Meanwhile, Fig. 6(b) shows that the reactive power ratio Q_{12}/P_{12} increases with the coupling coefficient k_C in an SS CPT compensation. Moreover, when the

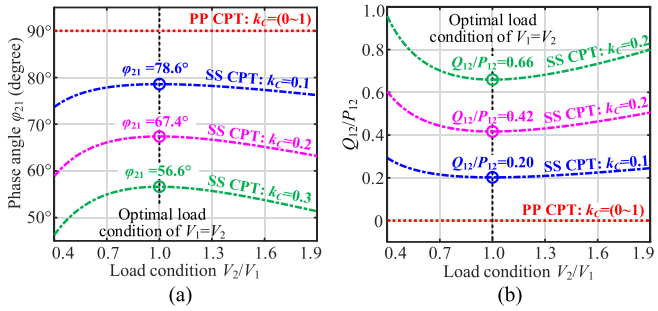

Fig. 7. Impact of load condition V_2/V_1 on (a) φ_{21} and (b) Q_{12}/P_{12}.

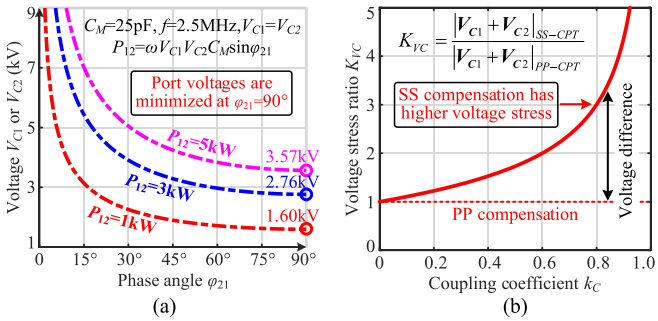

Fig. 8. (a) Impact of φ_{21} on plate voltage V_{C1} or V_{C2}. (b) E-field comparison between SS and PP CPT compensations.

load condition deviates from $V_1 = V_2$, φ_{21} and Q_{12}/P_{12} will further deteriorate, as shown in Fig. 7.

In a PP CPT compensation, $\boldsymbol{V_{C1}}$ and $\boldsymbol{V_{C2}}$, respectively, equal to $\boldsymbol{V_1}$ and $\boldsymbol{V_2}$, contributing to a constant 90° of φ_{21}, which is independent of k_C and load condition V_2/V_1, namely

$$\varphi_{21}|_{\text{PP}} = 90^\circ. \tag{5}$$

Due to the load- and k_C-independence, φ_{21} and Q_{12}/P_{12} of a PP CPT compensation, respectively, keep at desired values of 90° and zero, achieving zero reactive power circulating.

Overall, compared with an SS CPT compensation, in a PP compensation, the inductors L_{ex1} and L_{ex2} fully compensate the self-capacitance C_1 and C_2, respectively, as shown in the second row of Table II. This is the root reason why the PP compensation can achieve zero reactive power circulating and $\varphi_{21} = 90^\circ$.

Besides, φ_{21} also affects E-field emissions. For example, with $C_M = 25$ pF and $f = 2.5$ MHz, the voltages V_{C1} and V_{C2} versus φ_{21} are shown in Fig. 8(a). When $\varphi_{21} = 90^\circ$, V_{C1} and V_{C2} are minimized. In practice, the E-field emission is jointly determined by $\boldsymbol{V}_{C1}$ and $\boldsymbol{V}_{C2}$. The vector sums of $\boldsymbol{V}_{C1}$ and $\boldsymbol{V}_{C2}$ in SS and PP CPT compensations are defined as $V_{C\text{-SS}}$ and $V_{C\text{-PP}}$, respectively, quantifying E-field emission

$$\begin{aligned} V_{C-\text{SS}} &= |V_{C1} + V_{C2}|_{\text{SS}} \\ &= \left(1 + \frac{1}{k_C}\right)\sqrt{1 + (V_2/V_1)^2} \\ &\quad \times \sqrt{\frac{P_{12}}{(V_2/V_1)\omega C_M (1/k_C^2 - 1)}} \end{aligned} \tag{6}$$

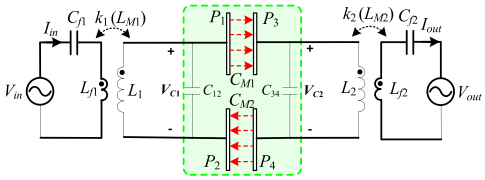

Fig. 9. Proposed M_1-PP-M_2 CPT circuit topology with simplified compensation (M_1 and M_2 represent the mutually coupled IPT links).

$$V_{C-\text{PP}} = |V_{C1} + V_{C2}|_{\text{PP}} = \sqrt{1 + (V_2/V_1)^2}\sqrt{\frac{P_{12}}{(V_2/V_1)\omega C_M}}. \tag{7}$$

The coefficient K_{VC} is defined to evaluate the difference in E-field emission of SS and PP CPT compensations, given in the following:

$$K_{VC} = \frac{V_{C-\text{SS}}}{V_{C-\text{PP}}} = \sqrt{\frac{1 + k_C}{1 - k_C}}. \tag{8}$$

It shows that a PP CPT compensation has a weaker E-field emission than an SS compensation, and this advantage becomes more significant as k_C increases, as shown in Fig. 8(b).

Three advantages of PP CPT compensation over a conventional SS compensation are summarized in the following.

First, a PP compensation achieves zero reactive power regardless of load and coupling conditions, maximizing active power P_{12} and eliminating reactive power loss.

Second, a PP compensation achieves weaker E-field emission at certain P_{12}, ω, and C_M. This advantage becomes more significant as k_C increases.

Third, a PP compensation permits a large k_C for high efficiency and design flexibility while an SS one has to select a small k_C (e.g., 0.1) to suppress Q_{21} and E-field emission [9].

III. Proposed M_1-PP-M_2 CPT System

A. Circuit Description

In Fig. 4. the capacitors C_{p1} and C_{p2} of SP IPT links are designed to resonate with inductors L_{ex1} and L_{ex2}, respectively, of the PP CPT circuit. Due to parallel resonance (open circuit), C_{p1}, C_{p2}, L_{ex1}, and L_{ex2} can be removed. Therefore, a simplified M_1-PP-M_2 CPT circuit topology is provided in Fig. 9.

B. Circuit Working Principle

In the proposed design, the double-sided SP IPT links are used to step-up coupler voltages V_{C1} and V_{C2} at ZPA frequency. They are tightly coupled and the coupling coefficients are defined as k_1 and k_2. L_{M1} and L_{M2} are the mutual inductances, defined in the following:

$$L_{M1} = k_1 \cdot \sqrt{L_{f1}L_1}, \quad L_{M2} = k_2 \cdot \sqrt{L_{f2}L_2}. \tag{9}$$

For the CPT circuit shown in Fig. 4, the operating frequency should synchronously satisfy the ZPA resonant conditions of both SP IPT and PP CPT circuits, provided in (10) and (11),

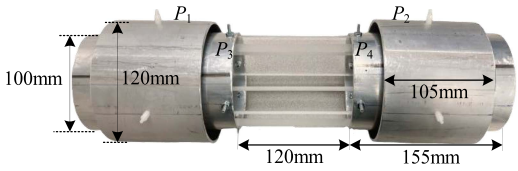

Fig. 10. Implemented sleeve-type capacitive coupler.

respectively [10], [11]. Considering the parallel resonance between C_{p1} and L_{ex1}, C_{p2}, and L_{ex2}, (12) is derived.

$$\omega|_{\text{SP-IPT}} = \frac{1}{\sqrt{C_{f1}L_{f1}(1-k_1^2)}} = \frac{1}{\sqrt{C_{p1}L_1}} = \frac{1}{\sqrt{C_{f2}L_{f2}(1-k_2^2)}} = \frac{1}{\sqrt{C_{p2}L_2}} \tag{10}$$

$$\omega|_{\text{PP-CPT}} = \frac{1}{\sqrt{L_{\text{ex1}}C_1}} = \frac{1}{\sqrt{L_{\text{ex2}}C_2}} \tag{11}$$

$$L_{\text{ex1}} = L_1, L_{\text{ex2}} = L_2. \tag{12}$$

According to (10)–(12), the resonant relationship of the simplified CPT topology in Fig. 9 is provided in the following:

$$\omega = \frac{1}{\sqrt{C_{f1}L_{f1}(1-k_1^2)}} = \frac{1}{\sqrt{L_1C_1}} = \frac{1}{\sqrt{L_2C_2}} = \frac{1}{\sqrt{C_{f2}L_{f2}(1-k_2^2)}}. \tag{13}$$

In resonant condition, the voltage step-up ratios of primary and secondary SP IPT links are defined as G_{V1} and G_{V2}. According to [11], G_{V1} and G_{V2} are given as follows:

$$G_{V1} = V_{C1}/V_{\text{in}} = L_1/L_{M1},$$
$$G_{V2} = V_{C2}/V_{\text{out}} = L_2/L_{M2}. \tag{14}$$

Then, a constant current output is achieved in the proposed M_1-*PP*-M_2 CPT system, as provided in the following:

$$I_{\text{out}} = V_{C1} \cdot j\omega C_M \cdot G_{V2} = V_{\text{in}} j\omega C_M \frac{L_1L_2}{L_{M1}L_{M2}}. \tag{15}$$

Therefore, the output power P_{out} is derived in the following:

$$P_{\text{out}} = V_{\text{out}}I_{\text{out}} = V_{C1}V_{C2}\omega C_M = V_{\text{in}}V_{\text{out}}\omega C_M \cdot \frac{L_1L_2}{L_{M1}L_{M2}}. \tag{16}$$

IV. Experimental Validation

A. Implementation of A 3.5-kW CPT System

A sleeve-type capacitive coupler is designed in Fig. 10. It is used for rotary applications, such as autonomous underwater vehicles. All plates have a 2-mm thickness, and the transfer distance is 8 mm. C_{M1} and C_{M2} are the main coupling capacitances while C_{p12} and C_{p34} represent parasitic shunt capacitances between coupler plates P_1 and P_2, P_3 and P_4. The Maxwell-simulated capacitances are provided in Table III, consistent with measurements.

System parameters are provided in Table IV, and the implemented prototype is shown in Fig. 11. The targeted power is 3.5 kW, the input voltage is 550 V, and the working frequency is 2.5 MHz. For the double-sided SP IPT links, the primary coils are inside the secondary ones, achieving a coupling coefficient of 0.63 and voltage gain G_{V1} (G_{V2}) of 6.0. L_{f1} is 5% larger than the designed value to achieve zero-voltage switching (ZVS). Externally parallel capacitors are used to construct C_{12} and C_{34}, achieving capacitance of 39 pF with a coupling coefficient of 0.39.

When the load resistance $R = 110\ \Omega$, the output power is 3.55 kW, and experimental waveforms are provided in Fig. 12. The input current I_{in} sightly lags V_{in}, achieving ZVS operation. The current I_{out} slightly leads V_{out}, which is attributed to the

TABLE III
Coupling Capacitance of the Designed Capacitive Coupler

Capacitance	C_{M1}/C_{M2}	C_{p12}	C_{p34}
Simulation	51.9pF	1.93pF	1.25pF
Measurement	50.0pF	*NaN*	*NaN*

TABLE IV
Parameters of the Implemented CPT Prototype

Parameter	Value	Parameter	Value
V_{dc}	550 V	f	2.5 MHz
MOSFET	C3M0120100K	Diode	C6D20065D
L_{f1}	4.7 μH	C_{f1}	1.5nF
L_{f2}	4.5 μH	C_{f2}	1.5nF
L_1	63.5 μH	L_2	63.7 μH
k_1, k_2	0.63	G_{V1}, G_{V2}	6.0
C_{M1}, C_{M2}	50.0pF	C_{12}, C_{34}	39.0pF
C_M	25.0 pF	C_1, C_2	64.0pF
Air gap	8 mm	k_C	0.391

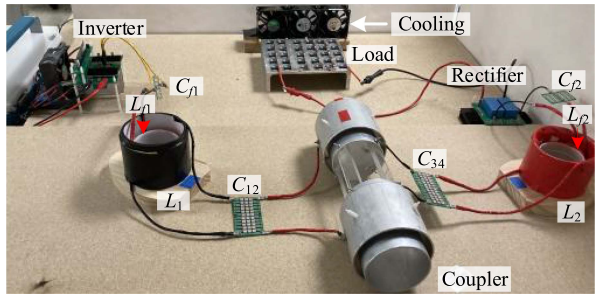

Fig. 11. Implemented 2.5-MHz 3.5-kW CPT prototype with passive components.

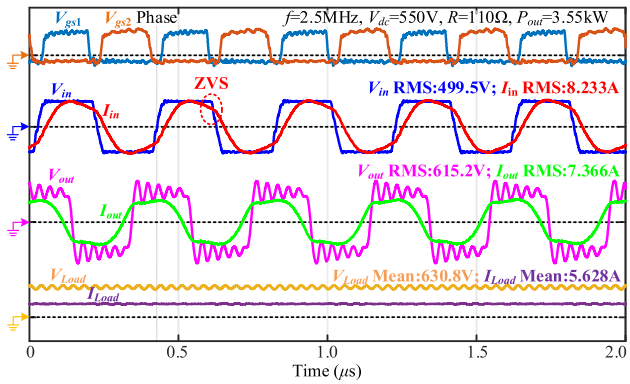

Fig. 12. Experimental waveforms of the CPT system at 3.55 kW and 2.5 MHz.

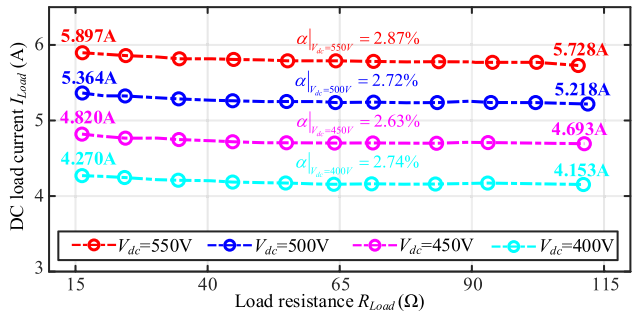

Fig. 13. Experimental results of DC output current $I_{\rm load}$ versus load resistance.

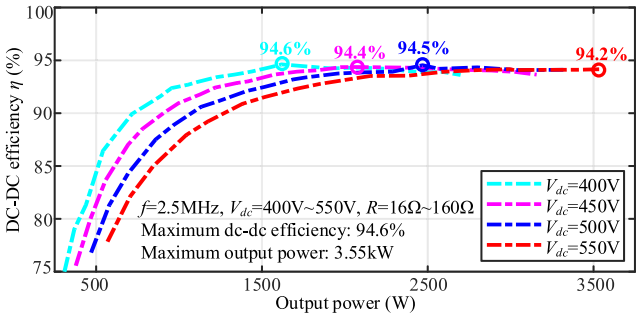

Fig. 14. Experimental power and efficiency performance.

parasitic capacitance of rectifier diodes. The parasitic inductance of the rectifier accounts for the slight oscillation of $V_{\rm out}$.

B. Load-Independent Constant-Current (CC) Output

With a wide load range of 16–110 Ω, the dc output current $I_{\rm load}$ is measured, as shown in Fig. 13. The current fluctuation ratio α is defined to evaluate the CC output property

$$\alpha = (I_{\rm max} - I_{\rm min})/I_{\rm max}. \tag{17}$$

It indicates that the current fluctuation ratio α is always smaller than 3% versus a large load variation of 587.5%, validating the CC output property.

C. Power and Efficiency Performance

The power and efficiency performance is tested at different load conditions, as shown in Fig. 14. The load resistance varies within 16–110 Ω, and the input voltage is within 400–550 V. The output power is 3.55 kW with 94.2% dc–dc efficiency when the load is 110 Ω, and the input voltage is 550 V. Besides, the maximum dc–dc efficiency of 94.6% is achieved when $V_{\rm dc} = 400$ V and $P_{\rm out} = 1.62$ kW.

With $f = 2.5$ MHz, $V_{\rm in} = 550$ V, and $P_{\rm out} = 3.55$ kW, the power loss distribution among circuit components is provided in Fig. 15. The coupler plates and compensation inductors L_1 and L_2 dissipate 33% and 21% of the power loss, respectively, significantly higher than other components. The future efficiency improvement will focus on increasing the quality factor of the capacitors and inductors as well as the multi-MHz inverter and rectifier optimization.

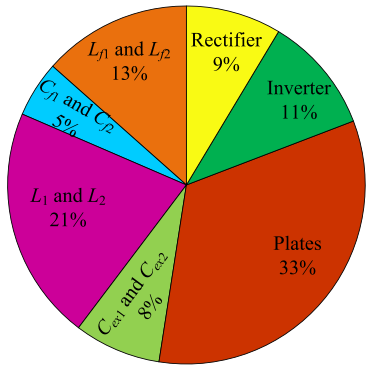

Fig. 15 Power loss distribution in components at 3.55 kW.

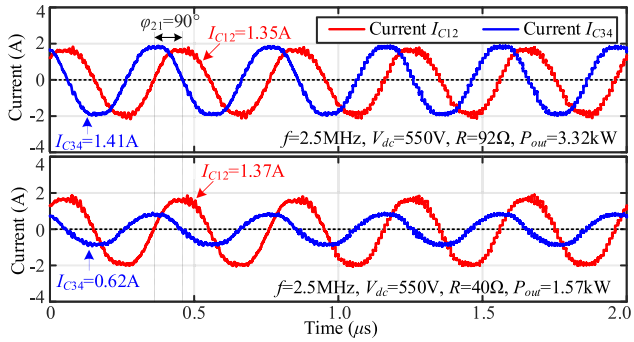

Fig. 16. Experimental current waveforms of capacitors C_{12} and C_{34}.

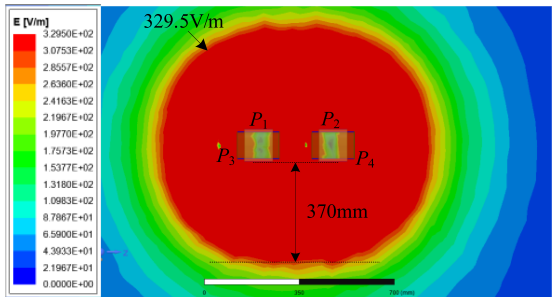

Fig. 17. Maxwell-simulated E-field distribution of a 3.55-kW CPT system.

D. Reactive Power Circulation and E-Field Emission

Considering the parasitic capacitance of a voltage probe, the waveforms of V_{C1} and V_{C2} cannot be directly captured by an oscilloscope. Therefore, the currents flowing through C_{12} and C_{34} are measured to demonstrate the phase relationship, as shown in Fig. 16. It shows that with different load conditions, I_{C12} (V_{C1}) always leads I_{C34} (V_{C2}) by 90°, validating the zero reactive power circulation property.

In this prototype, when the output power reaches 3.55 kW, the coupler voltages achieve $V_{C1} = 2.82$ kV and $V_{C2} = 3.32$ kV rms. According to the IEEE standard C95.1 [12], the E-field limit

is 329.52 V/m rms at 2.5 MHz. Based on the voltage stress, the simulated E-field distribution is shown in Fig. 17, indicating a safe distance of 370 mm at 3.55 kW output power.

Meantime, the voltages V_{CM1} and V_{CM2} can be calculated according to (18), which achieve 2.17 kV rms at 3.55 kW, meaning a peak value of 3.08 kV. Considering that the dielectric breakdown strength of air is at least 2 kV/mm, the insulation strength of the coupler plates is estimated to be 16 kV with an air gap of 8 mm, showing the safe working condition of the capacitive coupler.

$$|\boldsymbol{V}_{CM1}| = |\boldsymbol{V}_{CM2}| = \frac{|\boldsymbol{V}_{\boldsymbol{C}1} - \boldsymbol{V}_{\boldsymbol{C}2}|}{2} = \frac{\sqrt{|\boldsymbol{V}_{\boldsymbol{C}1}|^2 + |\boldsymbol{V}_{\boldsymbol{C}2}|^2}}{2}. \tag{18}$$

VI. Conclusion

This letter proposed a PP-based CPT system with double-side SP IPT links. The PP compensation aims at zero reactive power circulating in the capacitive coupler, thereby reducing the reactive power loss on capacitive coupler, maximizing the power transfer capability, and minimizing E-field emission at given working conditions. The double-side SP IPT links guarantee high power transfer by boosting the voltages of the capacitive coupler. A 2.5-MHz, 3.5-kW CPT prototype is implemented, and experimental results validate the targeted zero reactive power circulating property with 3.55 kW output power at 94.2% dc–dc efficiency, and the peak efficiency achieves 94.6% at 1.62 kW.

Acknowledgment

The views and opinions of authors expressed herein do not necessarily state or reflect those of the U.S. Government or any agency thereof.

References

[1] J. Dai and D. C. Ludois, "A survey of wireless power transfer and a critical comparison of inductive and capacitive coupling for small gap applications," *IEEE Trans. Power Electron.*, vol. 30, no. 11, pp. 6017–6029, Nov. 2015.

[2] D. Vincent, P. S. Huynh, N. A. Azeez, L. Patnaik, and S. S. Williamson, "Evolution of hybrid inductive and capacitive ac links for wireless EV charging—A comparative overview," *IEEE Trans. Transp. Electrific.*, vol. 5, no. 4, pp. 1060–1077, Dec. 2019.

[3] S. Li, Z. Liu, H. Zhao, L. Zhu, C. Shuai, and Z. Chen, "Wireless power transfer by electric field resonance and its application in dynamic charging," *IEEE Trans. Ind. Electron.*, vol. 63, no. 10, pp. 6602–6612, Oct. 2016.

[4] B. Regensburger, S. Sinha, A. Kumar, S. Maji, and K. K. Afridi, "High-Performance multi-MHz capacitive wireless power transfer system for EV charging utilizing interleaved-foil coupled inductors," *IEEE J. Emerg. Sel. Topics Power Electron.*, vol. 10, no. 1, pp. 35–51, Feb. 2022.

[5] F. Lu, H. Zhang, H. Hofmann, and C. Mi, "A double-sided LCLC-compensated capacitive power transfer system for electric vehicle charging," *IEEE Trans. Power Electron.*, vol. 30, no. 11, pp. 6011–6014, Nov. 2015.

[6] F. Lu, H. Zhang, H. Hofmann, and C. Mi, "A CLLC-compensated high power and large air-gap capacitive power transfer system for electric vehicle charging applications," in *Proc. IEEE Appl. Power Electron. Conf. Expo.*, 2016, pp. 1721–1725.

[7] H. Zhang, F. Lu, H. Hofmann, W. Liu, and C. C. Mi, "Six-plate capacitive coupler to reduce electric field emission in large air-gap capacitive power transfer," *IEEE Trans. Power Electron.*, vol. 33, no. 1, pp. 665–675, Jan. 2018.

[8] L. Li, Z. Wang, F. Gao, S. Wang, and J. Deng, "A family of compensation topologies for capacitive power transfer converters for wireless electric vehicle charger," *Appl. Energy*, vol. 260, 2020, Art. no. 114156.

[9] J. Xia, X. Yuan, S. Lu, J. Li, S. Luo, and S. Li, "A two-stage parameter optimization method for capacitive power transfer systems," *IEEE Trans. Power Electron.*, vol. 37, no. 1, pp. 1102–1117, Jan. 2022.

[10] Y. Wang, H. Zhang, and F. Lu, "Review, analysis, and design of four basic CPT topologies and the application of high-order compensation networks," *IEEE Trans. Power Electron.*, vol. 37, no. 5, pp. 6181–6193, May 2022.

[11] Y. H. Sohn, B. H. Choi, E. S. Lee, G. C. Lim, G. Cho, and C. T. Rim, "General unified analyses of two-capacitor inductive power transfer systems: Equivalence of current-source SS and SP compensations," *IEEE Trans. Power Electron.*, vol. 30, no. 11, pp. 6030–6045, Nov. 2015.

[12] *IEEE Standard for Safety Levels with Respect to Human Exposure to Radio Frequency Electromagnetic Fields, 3 kHz to 300 GHz*, IEEE Standard C95.1, 2005.